



HAL
open science

Self-Aggregation of Convective Clouds With Interactive Sea Surface Temperature

Sara Shamekh, Caroline Muller, Jean Philippe Duvel, Fabio d'Andrea

► **To cite this version:**

Sara Shamekh, Caroline Muller, Jean Philippe Duvel, Fabio d'Andrea. Self-Aggregation of Convective Clouds With Interactive Sea Surface Temperature. *Journal of Advances in Modeling Earth Systems*, 2020, 10.1029/2020MS002164 . hal-03023326

HAL Id: hal-03023326

<https://hal.science/hal-03023326>

Submitted on 25 Nov 2020

HAL is a multi-disciplinary open access archive for the deposit and dissemination of scientific research documents, whether they are published or not. The documents may come from teaching and research institutions in France or abroad, or from public or private research centers.

L'archive ouverte pluridisciplinaire **HAL**, est destinée au dépôt et à la diffusion de documents scientifiques de niveau recherche, publiés ou non, émanant des établissements d'enseignement et de recherche français ou étrangers, des laboratoires publics ou privés.

1 **Self-aggregation of convective clouds with interactive**
2 **sea surface temperature**

3 **S. Shamekh¹, C. Muller¹, J-P. Duvel¹, F. D'Andrea¹**

4 ¹Laboratoire de Météorologie Dynamique IPSL, École Normale Supérieure, PSL Research University,
5 CNRS, Paris, France

Corresponding author: Sara Shamekh, Shamekh@lmd.ens.fr

Abstract

This study investigates the feedbacks between an interactive sea surface temperature (SST) and the self-aggregation of deep convective clouds, using a cloud-resolving model in non-rotating radiative-convective equilibrium. The ocean is modeled as one layer slab with a temporally fixed mean but spatially varying temperature. We find that the interactive SST decelerates the aggregation, and that the deceleration is larger with a shallower slab, consistent with earlier studies. The surface temperature anomaly in dry regions is positive at first, thus opposing the diverging shallow circulation known to favor self-aggregation, consistent with the slower aggregation. But surprisingly the driest columns then have a negative SST anomaly, thus strengthening the diverging shallow circulation and favoring aggregation. This diverging circulation out of dry regions is found to be well correlated with the aggregation speed. It can be linked to a positive surface pressure anomaly (PSFC), itself the consequence of SST anomalies and boundary layer radiative cooling. The latter cools and dries the boundary layer, thus increasing PSFC anomalies through virtual effects and hydrostasy. Sensitivity experiments confirm the key role played by boundary layer radiative cooling in determining PSFC anomalies in dry regions, and thus the shallow diverging circulation and the aggregation speed.

Plain Language Summary

Convective clouds can organize into large clusters, such as those observed during the Madden-Julian oscillation, or tropical cyclones. Interactions between Sea Surface Temperature (SST) and the atmosphere impact the development of these organizations. Using a high-resolution atmospheric model coupled to an interactive sea surface, we investigate what physical processes lead to the development of the convective organization and how SST impacts these processes. We find that, in the clear-sky regions, the formation of a higher pressure drives a near-surface flow from clear-sky to the cloudy regions. This flow transports moisture to an already moist region, dries further the clear-sky regions and prevents cloud formation there. This process leads to the expansion of the clear-sky regions, thus confinement of convective clouds to a smaller moist region. The high-pressure anomaly is due to the cooling and drying of the atmosphere that makes the air denser. This atmospheric cooling and drying is controlled by radiation and SST anomalies. The formation of higher pressure is first opposed by warmer SST, and then favored by colder SST as the clear sky region becomes drier and drier. In response to the high-pressure anomaly, the near-surface flow forms and drives the organization of convective clouds into a moist cluster.

1 Introduction

The spontaneous organization of deep convective clouds into a single cluster, which is known as self-aggregation, has been found across a wide range of 2D and 3D cloud-resolving models (CRMs) and global climate models (GCMs) with different configurations and domain shapes and sizes (Nakajima & Matsuno, 1988; Held et al., 1993; Muller & Held, 2012; Wing et al., 2017; Wing, 2019). Self-aggregation typically starts with the appearance and growth of persistent dry areas devoid of deep convection. The growth of those dry regions leads to the confinement of convection to a remaining small fraction of the simulation domain. This phenomenon results in a reduction of domain-averaged water vapor content, and consequently a significant enhancement of outgoing longwave radiation to space. If relevant to the real world, this self-aggregation of deep convective clouds could potentially impact the climate sensitivity (Mauritsen & Stevens, 2015; Coppin & Bony, 2018).

53 Several studies have investigated the physical processes responsible for this phe-
 54 nomenon. Most of these studies use fixed sea-surface temperature (SST). In a seminal
 55 study, Bretherton et al. (2005) point out the importance of surface fluxes and atmospheric
 56 radiative cooling for self-aggregation. They find that enhanced radiative cooling in the
 57 lower troposphere in dry regions leads to the formation of a shallow flux from dry to moist
 58 regions. This shallow circulation transports moist static energy (MSE) from dry to moist
 59 regions, i.e. up-gradient (from low MSE to high MSE regions), thus reinforcing the MSE
 60 gradient and the aggregation of convection.

61 The importance of atmospheric radiative cooling has been confirmed by other stud-
 62 ies as well, however, based on model and simulation configuration, different radiative feed-
 63 backs can drive the self-aggregation. Muller and Held (2012) show that the low-level clouds
 64 longwave radiation is necessary for self-aggregation to occur from homogeneous initial
 65 conditions, while clear-sky and high-clouds longwave radiative feedbacks are sufficient
 66 to maintain the aggregation. Yang (2018) mentions the importance boundary layer mois-
 67 ture variance and boundary layer differential radiative cooling. Wing and Emanuel (2014)
 68 also highlight the importance of clear-sky free-tropospheric radiative cooling. Other stud-
 69 ies mention the importance of free-tropospheric moisture and convection-moisture feed-
 70 back (Tompkins & Craig, 1998; Craig & Mack, 2013), surface fluxes feedbacks (Coppin
 71 & Bony, 2015), and also cold pool-convection feedback (Jeevanjee & Romps, 2013). In
 72 summary, several physical processes contribute to the onset and maintenance of convective
 73 self-aggregation. It is still unclear which one of those feedbacks, if any, dominates.
 74 In particular, more work is desirable to clarify the role of low-level versus free-tropospheric
 75 radiative feedbacks on driving self-aggregation.

76 One robust feature though, is the significant increase of MSE variance with self-
 77 aggregation (Wing & Emanuel, 2014). As mentioned above, the radiatively-driven shal-
 78 low circulation, and concomitant up-gradient MSE transport, are believed to play a key
 79 role. Indeed, the shallow circulation transports low level air with high MSE to already
 80 moist regions. A strong shallow flux can result in a strong up-gradient transport of MSE,
 81 thus negative gross moist stability, which is known to favor aggregation (Bretherton et
 82 al., 2005). The importance of boundary-layer differential radiative cooling rates, between
 83 dry and moist regions, in driving this shallow circulation has been suggested by Muller
 84 and Bony (2015). Using a conceptual, analytical model of the boundary layer, Naumann
 85 et al. (2017) and Naumann et al. (2019) further investigate the divergent shallow circula-
 86 tion out of a dry region driven by enhanced boundary layer radiative cooling, and how
 87 it compares to the shallow circulation driven by SST anomalies. Their dry theoretical
 88 model confirms that a shallow circulation can be maintained for differences in radiative
 89 boundary-layer cooling rates larger than 1 K day^{-1} . The circulation strength is compa-
 90 rable to that caused by SST differences of a few kelvins (Naumann et al., 2017), or even
 91 larger when moisture effects are accounted for (Naumann et al., 2019). The circulation
 92 follows from colder boundary layer temperatures, and thus increased hydrostatic surface
 93 pressures, in regions with larger boundary layer radiative cooling.

94 Worth to mention that all the studies mentioned so far used fixed homogeneous sur-
 95 face temperature. Using a non-homogeneous SST (constant in time but inhomogeneous
 96 in space) or an interactive SST (evolving in time) can also change the occurrence of self-
 97 aggregation and the dominating feedback (Tompkins, 2001; Liu & Moncrieff, 2008; Ho-
 98 henegger & Stevens, 2016; Shamekh et al., 2019; Miller & Hohenegger, 2020). Introduc-
 99 ing an SST anomaly can dictate the preferred location of convection (Tompkins, 2001)
 100 and thus impact the self-aggregation. When a circular SST anomaly (constant in time)
 101 is imposed, the aggregation process is significantly accelerated (Shamekh et al., 2019),
 102 due to the large-scale circulation that develops in response to the stronger upward mass
 103 flux over the warm region. Consistently, Back and Bretherton (2009) show that a bound-

104 ary layer divergent flow forms in response to an SST gradient, that can re-enforce deep
 105 convection.

106 A few studies have also investigated the response of self-aggregation to an inter-
 107 active SST. In that case, the SST evolves in space and time according to the local en-
 108 ergy budget (see section 2.3 for more details). When SST is allowed to interact with the
 109 atmosphere, the self-aggregation is typically delayed or prevented (Hohenegger & Stevens,
 110 2016; Grabowski, 2006; Coppin & Bony, 2017). Using a GCM coupled with a slab ocean,
 111 Grabowski (2006) shows that warm SST anomalies form under the cloud free area by
 112 enhanced shortwave radiation which reaches the surface. In the GCM, convective clus-
 113 ters follow the warm SST anomaly, and results in an easterly propagating convective clus-
 114 ter similar to the Madden Julian oscillation (Arnold & Randall, 2015). In a similar set-
 115 up, Coppin and Bony (2017) find that the convective aggregates prefer to stay on the
 116 maximum of SST gradient, which also results in the similar propagation found by Grabowski
 117 (2006).

118 Using a cloud resolving model and a domain of $(576 \text{ km})^2$, Hohenegger and Stevens
 119 (2016) investigate the impact of different slab depths on the aggregation of convection.
 120 They find that the coupling between the SST and the atmosphere delays the onset of
 121 self-aggregation, or prevents it completely if the slab is very shallow (1 m). They sug-
 122 gest that this delay is the result of the formation of an SST gradient, which opposes the
 123 boundary layer divergent flow (shallow circulation mentioned above) known to be im-
 124 portant for the development of convective aggregation, a hypothesis that we further in-
 125 vestigate and quantify here. Of particular interest are the following questions:

- 126 • What is the impact of interactive SST on aggregation, and how do surface vari-
 127 ables evolve as the aggregation progresses?
- 128 • Do SST anomalies oppose the shallow circulation between dry and moist regions?
- 129 • What is the relative importance of the shallow versus the deep circulation in the
 130 MSE transport and time scale of aggregation?

131 The next section describes the CRM and simulations in more detail, as well as the
 132 index used to quantify the convective aggregation. Section 3 describes the impact of in-
 133 teractive SST on aggregation for various slab depths and mean SST, and describes in
 134 detail the evolution of surface properties in one simulation. Section 4 investigates the
 135 physical processes behind the sensitivity to mixed layer depth and domain-mean SST,
 136 notably the relative roles of boundary layer radiative cooling anomalies and SST anom-
 137 alies in setting up a shallow circulation. Concluding remarks are offered in §5.

138 2 Method

139 2.1 Cloud-resolving model

140 The CRM used is the model System for Atmospheric Modeling (SAM) version 6.11.1
 141 (Khairoutdinov & Randall, 2003). This model solves the anelastic equations of conser-
 142 vation of momentum, water (with 6 species present in the model, water vapor, cloud liq-
 143 uid, cloud ice, precipitating rain, precipitating snow, and precipitating graupel), and en-
 144 ergy. The relevant energy for moist convection is the moist static energy (MSE), as it
 145 is conserved (approximately, i.e. neglecting viscous and subgrid-scale effects) under adi-
 146 abatic processes including the phase change of water. More precisely in this model, the

147 so-called "frozen" MSE is conserved during moist adiabatic processes, including the freez-
 148 ing of precipitation. The frozen MSE is given by

$$MSE = c_p T + gz + L_v q - L_f q_{ice}, \quad (1)$$

149 with the specific heat capacity of air at constant pressure c_p , temperature T , gravity g ,
 150 height z , latent heat of evaporation L_v , water vapor specific humidity q_v , latent heat of
 151 fusion L_f , and specific humidity of all ice phase condensates q_{ice} .

152 The subgrid-scale turbulence is modeled using a Smagorinsky-type parameteriza-
 153 tion, and we use the 1-moment microphysics formulation, following Bretherton et al. (2005)
 154 and Muller and Held (2012). Surface fluxes are computed using bulk formulae. Further
 155 information about the model can be found in Khairoutdinov and Randall (2003).

156 All simulations use interactive radiation, using the radiation code from the National
 157 Center for Atmospheric Research (NCAR) Community Atmosphere Model version 3 (CAM3;
 158 Collins et al., 2006). For simplicity, we neglect the diurnal cycle and use the daily mean
 159 incoming solar insolation of 413 W m^{-2} (same setting as Tompkins & Craig, 1998).

160 2.2 Experimental setup

161 The model domain is square, doubly-periodic in both horizontal directions x and
 162 y . We run simulations with horizontal domain size $(576 \text{ km})^2$. The horizontal resolution
 163 is 3 km and the vertical grid spacing increases gradually with height, with the first level
 164 at 25 m and a resolution of 50 m close to the sea surface, reaching a vertical resolution
 165 of 500 m in the mid troposphere. There are 64 vertical levels which span 27 km in the
 166 vertical. This includes a sponge layer in the upper third of the domain (from $z = 18$
 167 km to 27 km) where the wind is relaxed to zero in order to reduce gravity wave reflec-
 168 tion and buildup. No large-scale forcing or wind is imposed in the domain. We neglect
 169 the Earth's rotation, a reasonable approximation in the tropics where the Coriolis pa-
 170 rameter is small.

171 The initial conditions for the different domain averaged SSTs are obtained from
 172 smaller domain runs with the corresponding SST at radiative-convective equilibrium (RCE)
 173 $((96 \text{ km})^2$ run to 50 days), then using time and domain averaged profiles of the last 5
 174 days. We run simulations with three different depths of slab: $H = 5, 10,$ and 50 meters,
 175 at two domain-averaged SSTs = 300 and 305 K. This allows us to explore the impact
 176 of interactive SST on aggregation, and compare the sensitivity to slab depth to the im-
 177 pact of changing domain-averaged SST by 5 K. We also perform fixed SST simulations
 178 for both SST = 300 and 305. Note that fixed SST is mathematically equivalent to in-
 179 finite slab depth, thus the results should converge to the fixed SST simulation when H
 180 increases. A simulation will be referred to by its depth of slab and its SST so that, for
 181 example, simulation H5SST305 has slab depth of 5 meters and SST = 305 K.

182 As the time to equilibrium is longer with interactive SST, and thus the computa-
 183 tion is more expensive, in particular with shallow slab depth, we stop the simulations
 184 when the metric used for the aggregation progress (introduced below in §2.4) reaches its
 185 maximum and drops back down to its equilibrium value. Worth to mention that after
 186 this drop, the metric oscillates around a value between 0.4-0.5 and does not depend on
 187 slab depth or mean SST.

188

2.3 Slab ocean

189

190

191

192

193

194

195

196

One technical complication with tropical simulations using interactive SST, is that the incoming solar radiation in the tropics exceeds the threshold for a runaway greenhouse gas warming (Pierrehumbert, 2010). In the tropics, oceanic and atmospheric transport of energy out of the tropics compensates the energy imbalance at the top of the atmosphere and prevents excessive warming. This is not the case in simulations of an isolated tropical region with periodic boundary conditions that lacks the transport of energy out of the tropics by the [Hadley cell and mean ocean circulation, as well as eddy transport](#).

197

198

199

200

Several solutions have been proposed to overcome this issue, e.g. reducing the incoming solar flux (Cronin et al., 2015), adding a constant deep ocean flux (Romps, 2011), or relaxing the domain average SST to a target temperature (Semie & Tompkins, 2016) i.e. adding a deep ocean flux which ensures little drift in domain-mean SST.

201

202

203

204

205

206

207

208

Aggregation is known to be sensitive to the domain-mean SST (e.g., Wing & Emanuel, 2014). Thus in order to separate the effects of domain-mean SST and of spatial inhomogeneities, here we follow Semie and Tompkins (2016) and relax the domain-averaged ocean mixed layer temperature \overline{SST} toward a fixed target temperature SST_0 (see Appendix A for a brief discussion of simulations with a constant deep ocean flux and their domain mean SST drifts). This relaxation method allows us to keep the domain-averaged SST constant over time while it allows the SST to vary locally according to the evolution equation:

$$\rho_w c_{p,w} H \left(\frac{dSST}{dt} + \frac{\overline{SST} - SST_0}{\tau_0} \right) = Q_{SW}^N + Q_{LW}^N + LHF + SHF \quad (2)$$

209

210

211

212

213

214

215

where ρ_w denotes water density, $c_{p,w}$ is the specific heat capacity of water at constant pressure, H the depth of the slab, τ_0 the relaxation time scale, which is constant and equal to two hours in all of our simulations (this value was empirically determined to avoid significant drift in the domain mean SST). All the terms on the right hand side of 2 are positive downward (increase SST) and negative upward (decrease SST). LHF and SHF denote surface latent and sensible heat fluxes (up to a minus sign), and Q_{SW}^N and Q_{LW}^N stand respectively for shortwave and longwave net radiative flux at the surface, with

$$Q_{LW}^N = LW_d - \sigma SST^4, \quad (3)$$

216

217

where σ is the Stephen-Boltzmann constant and LW_d the downward longwave flux at the surface.

218

Also

$$Q_{SW}^N = (1 - \alpha) SW_d = (1 - \alpha) SW_{TOA} e^{(-\tau/\mu_0)} \quad (4)$$

219

220

221

222

223

where α is albedo, SW_d is downward shortwave flux at the surface, μ_0 is a constant which depends on the zenith angle, τ is the shortwave optical depth, and SW_{TOA} is the incoming shortwave flux at the top of the atmosphere. In our simulations, τ changes only by changes in water vapor and cloud water content of the atmosphere as the other ingredients do not change.

224

225

Using equation 2, we can find an equation for spatial SST anomalies $SST' = SST - \overline{SST}$:

$$\frac{dSST'}{dt} = \frac{1}{\rho_w c_{p,w} H} \left(Q_{SW}'^N + Q_{LW}'^N + LHF' + SHF' \right) \quad (5)$$

226 Worth to mention that the relaxation term disappears as it is the same everywhere in
 227 the domain. Thus the spatial variability of SST arises from spatial variations of the en-
 228 ergy flux at the surface.

229 2.4 Analysis Framework

230 To follow the progress of aggregation we use column relative humidity CRH (Wing
 231 & Cronin, 2016; Shamekh et al., 2019).

$$CRH = \frac{\int q_v \rho dz}{\int q_{v,sat} \rho dz}, \quad (6)$$

232 where $q_{v,sat}$ is the saturation water vapor specific humidity, ρ the air density and the ver-
 233 tical integration is done over the troposphere. We use CRH for our analysis as it is less
 234 dependent on surface temperature compared to the integrated column water vapor (PW),
 235 thus it allows us to compare the aggregation progress at different SSTs.

236 In our simulations, deep convection does not occur in regions with $CRH < 0.6$,
 237 thus, we define the dry patch as the area with $CRH < 0.6$. With the progress of ag-
 238 gregation, these dry patches grow and merge so that they take a larger and larger frac-
 239 tion of the domain. As the growth of the dry patches is the main feature in all our sim-
 240 ulations, to follow the progress of aggregation, we use the fractional area covered by dry
 241 patches, which we will refer to as the aggregation index.

242 3 The impact of interactive SST on the aggregation of convective clouds

243 In this section, we first provide an overview of the main results regarding the im-
 244 pact of interactive SST on the progress of self-aggregation in our simulations. We then
 245 study in detail one simulation with slab depth = 5 m and domain mean SST = 305 K
 246 (hereafter H5SST305) as processes are found to be qualitatively similar in all simulations.
 247 Notably, we investigate in detail how interactive surface temperatures affect the surface
 248 pressure anomaly in dry regions, and thus the shallow circulation between dry and moist
 249 regions known to play an important role in the aggregation process.

250 3.1 Overview of results

251 Figure 1 shows the aggregation index for the simulations with interactive SST with
 252 different slab depths and with SSTs 300 and 305 K. To compare the timing of self ag-
 253 gregation in our simulations, we simply compare the time at which the aggregation in-
 254 dex reaches its maximum (Figure 1).

255 Generally speaking, introducing a slab ocean with interactive surface temperature
 256 delays self-aggregation (Figure 1). Consistently, the fixed SST simulations (which cor-
 257 respond to infinite slab depth) are faster at both 300 K and 305 K than the interactive
 258 SST simulations with the same mean SST. This is consistent with previous studies on
 259 the impact of slab ocean on self-aggregation (Hohenegger & Stevens, 2016; Bretherton
 260 et al., 2005). Here, with the slab depths that we examined, the aggregation always pro-
 261 ceeds, but it is significantly delayed with a shallow slab as, for example H10SST305 and
 262 H5SST305 delay the self-aggregation by 12 and 25 days respectively compared to fixed
 263 SST simulation (Figure 1). The delays obtained with interactive SST (tens of days) are

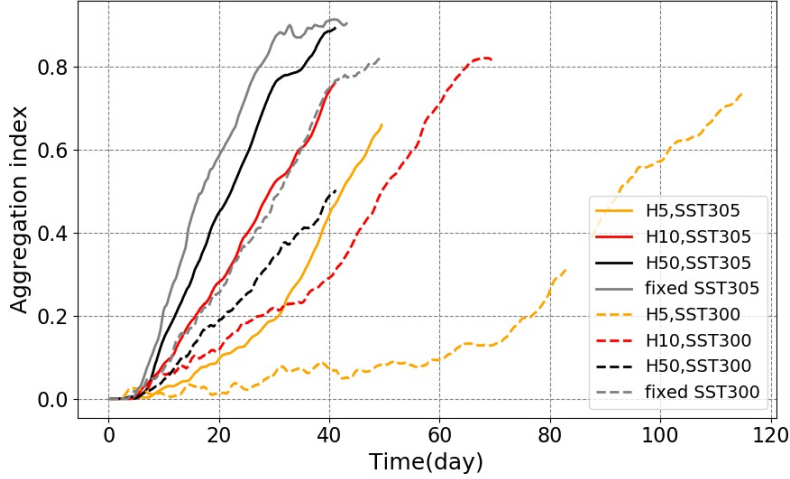


Figure 1. Time series of the aggregation index ($\text{Area}_{CRH < 0.6}$) for $SST_0 = 300K$ (dashed lines) and $SST_0 = 305K$ (plain lines) and different slab depths. Simulations with fixed SST are also shown for reference (gray lines). (We note in passing that the few days missing in the H5SST300 simulation, around day 85, are due to a technical issue, but do not affect the results discussed here.)

264 comparable to the delays obtained when reducing the SST. Indeed, similar tens of days
 265 delays are found when decreasing the SST from 305 to 300 K for a given slab depth (Fig-
 266 ure 1).

267 Note that in some of the simulations, there is a period of slower increase of the ag-
 268 gregation index (e.g. H5SST300 before day 70, or H5SST305 before day 30) before the
 269 index starts its faster monotonic increase. We refer to this delayed period, for which the
 270 aggregation index is not increasing significantly, as latency.

271 We now investigate in more detail surface properties in one of the simulations since,
 272 as mentioned earlier, properties are found to be qualitatively robust in all the runs. Of
 273 particular interest are the evolution of surface temperature and surface pressure in dry
 274 regions, and how these impact the circulation.

275 3.2 SST anomalies

276 Figure 2 shows the time evolution of several variables, including SST anomaly and
 277 the surface energy budget anomaly (right hand side of equation 5) in the simulation H5SST305.
 278 The first dry patches are well detectable at day 16 (Figure 2.a). These dry patches grow
 279 where they firstly appear without significant displacement. By day 40, a single circular
 280 dry patch exists and covers half of the domain. Worth to mention that the dryness is
 281 more pronounced in the free troposphere, specially at early time, and reaches the bound-
 282 ary layer by day 24 (Figure 3).

283 We see that the SST anomalies exhibit two different stages of evolution: 1. an early
 284 stage warming which happens when the dry patch is newly formed and still has large amount
 285 of column water vapor, so that shortwave warming dominates; 2. a later stage cooling

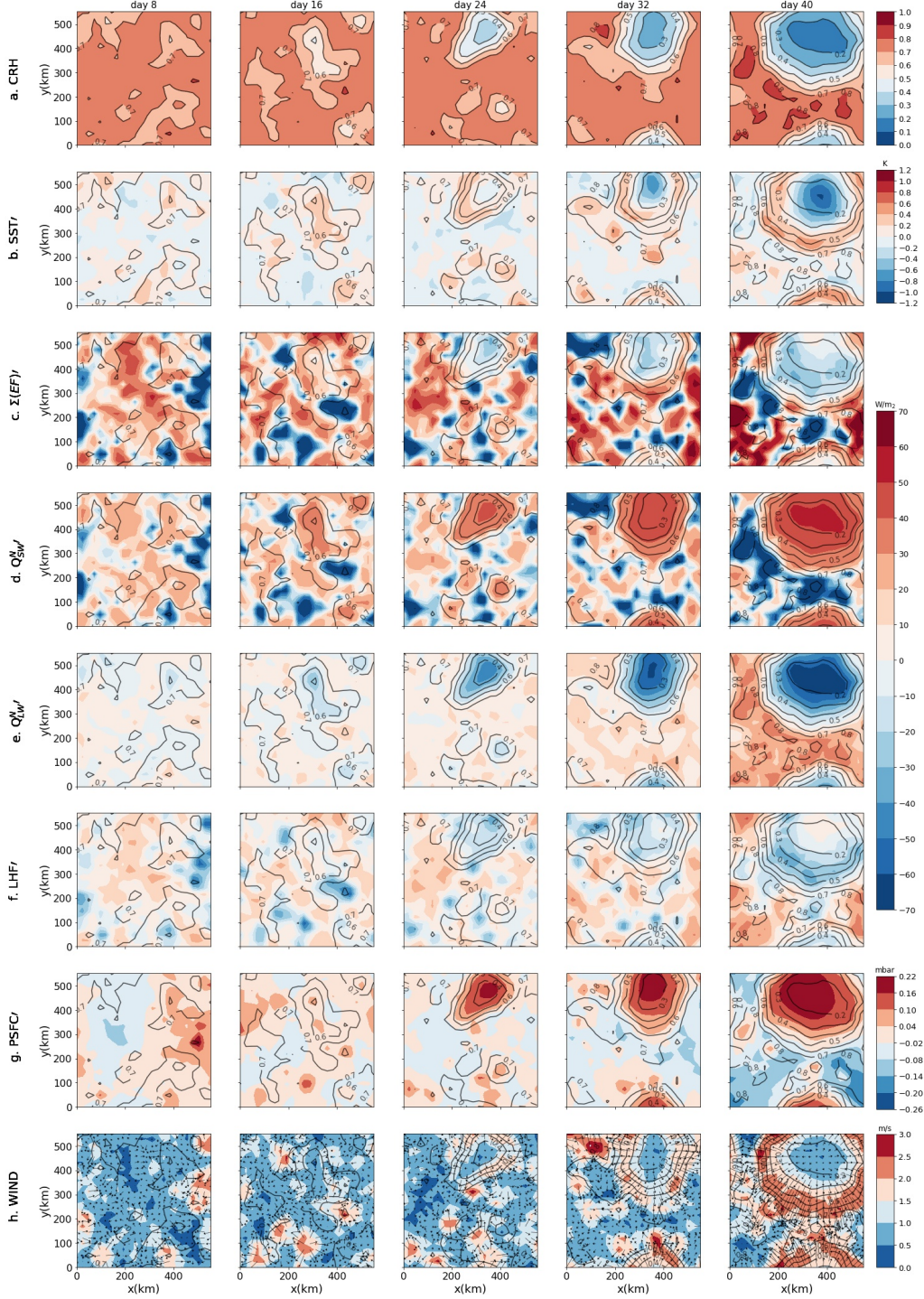


Figure 2. The rows show daily mean of: a) CRH, b) SST anomaly, c) Net energy flux at the surface, d) net shortwave radiative flux anomaly at the surface, e) net longwave radiative flux anomaly at the surface, f) surface latent heat flux anomaly, g) surface pressure anomaly, and h) surface wind (color) with arrows showing the direction of the wind. Columns show the time progress of each variable. The data are taken from the simulation H5SST305 averaged over 6 hours of the day mentioned on the top of each column. Each panel is further smoother by 16×16 grids column averaging. The contours of CRH are repeated in all panels to ease comparison. In all flux plots (c, d, e, and f) downward (upward) flux is shown with positive (negative) sign.

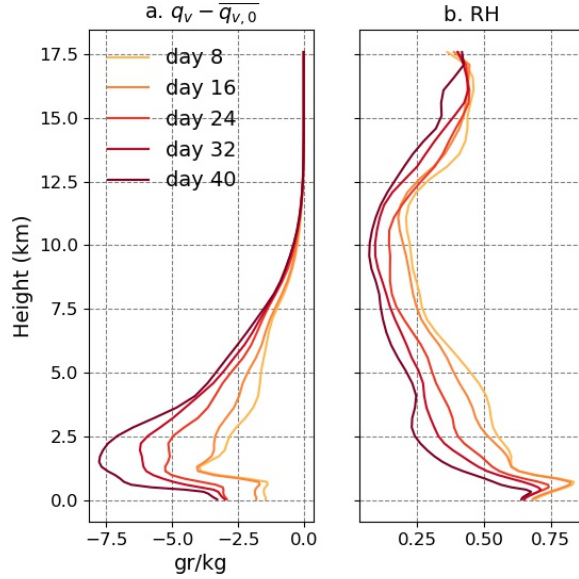


Figure 3. The vertical profiles of a) total change in specific humidity ($q_v - \overline{q_{v,0}}$) and b) relative humidity averaged over the dry patch (defined by $CRH < 0.6$) for the simulation H5SST305.

286 at the center of the dry patch surrounded by a ring of warm water which is located at
 287 the edge of the dry patch. This pattern appears with further dryness of the dry patch,
 288 so that longwave cooling dominates at the center of the dry patch; [worth to mention that](#)
 289 [the dry patches become cloud free from early time \(see Figure 2.d\)](#). In the following we
 290 investigate each of these stages separately.

291 a. Early stage warming

292 The temperature anomaly underneath the dry patches at their early appearance
 293 (up to day 16) is positive, thus the first impact of a dry patch on the surface temper-
 294 ature is warming (Figure 2.b). This early stage warming in dry regions can be under-
 295 stood by looking at the net energy flux anomaly (hereafter $\Sigma E F'$) at the surface (Equa-
 296 tion 5 and Figure 2.c). In dry regions, $\Sigma E F'$ is initially positive, thus leading to an SST
 297 increase with time. $\Sigma E F'$ is predominantly determined by shortwave and longwave ra-
 298 diative fluxes at the surface, with also a small contribution by surface latent heat flux.
 299 The sensible heat flux is very small thus negligible.

300 The early stage warming is mainly because of an enhancement in the shortwave ra-
 301 diative flux at the surface (SWNS), as the dry patches become cloud free and more trans-
 302 parent from the very beginning, letting larger amounts of shortwave radiation reach the
 303 surface and building up positive SST anomalies locally (Figure 2.b and d). These cloud
 304 free dry patches experience a reduction in total column water vapor (Figure 3). As noted
 305 above, the dryness starts from the free troposphere and is not significant in the bound-
 306 ary layer (up to day 16).

307 When the free troposphere becomes dry, the boundary layer and the surface can
 308 radiatively cool more efficiently in the longwave (Emanuel et al., 2014). The enhance-

309 ment of net longwave radiative flux at the surface (LWNS) is clear in Figure 2.e, how-
 310 ever, as the dry patches still have a large amount of water vapor, especially in the bound-
 311 ary layer, the surface cooling by LWNS is smaller than warming by enhanced shortwave
 312 radiative flux. All together, at early stage of dry patches, surface warming by SWNS is
 313 more efficient compared to cooling by LWNS (and LHF) leading to the formation of warm
 314 SST anomalies.

315 **b. Later stage cooling**

316 By day 24, with further dryness and expansion of the dry patches, surprisingly the
 317 surface at the center of one of the dry patches with lowest CRH becomes colder than the
 318 area around it (Figure 2.b, the dry patch at $x=400$ km and $y=500$ km) so that a cold
 319 anomaly surrounded by a ring of warm water forms. CRH over the ring of warm water
 320 is large (roughly comparable with CRH in the dry patches at day 16) thus its warming
 321 is caused by the dominance of SWNS versus LWNS and LHF. The cooling at the center
 322 of the dry patch indicates that further drying of the dry patches can have a cooling
 323 effect on the surface temperature underneath them by increasing LWNS with an addi-
 324 tional albeit small contribution from enhanced LHF. The surface latent heat fluxes (Fig-
 325 ure 2.f) increases as a result of increased gradient of specific humidity between the sur-
 326 face and the first layer of the atmosphere, as the dryness has already reached the bound-
 327 ary layer (Figure 3), further enhanced by surface winds in the ring around the cold anomaly
 328 (Figure 2.h). The enhanced LWNS is the result of low amount of column water vapor
 329 that results in a smaller downward longwave radiative flux at the surface and allows the
 330 LWNS to increase. This enhancement is well seen in Figure 2.e, day 24 at $x=400$ km and
 331 $y=500$ km.

332 To summarize, at the center of the dry patch, around day 24, cooling by LWNS dom-
 333 inates (and LHF) results in a negative trend in surface temperature anomaly, while at
 334 the edge of the dry patch, shortwave warming overcomes longwave cooling (and the small
 335 contribution from latent heat flux) so that a ring of warm water forms. This pattern of
 336 warm ring-cold center further intensifies with dryness of dry patch. By day 40, LHF at
 337 the center of the dry patch reduces due to the reductio of SST and small surface wind.
 338 At this stage, the cold patch persists as LWNS remains larger than SWNS and LHF.

339 After day 40, the reduction in LHF results in an increase in surface temperature
 340 anomaly at the center of the dry patch (not shown). The warmer center in return in-
 341 creases LHF, so that the SST anomaly and LHF at the center of the dry patch oscillate
 342 slowly around an equilibrium value (not shown).

343 These SST anomalies can potentially affect the aggregation speed by impacting the
 344 surface pressure anomaly in dry regions, an aspect which we further investigate in the
 345 following section.

346 **3.3 Surface pressure anomaly**

347 At the early stage of the simulation, the surface pressure anomaly (hereafter PSFC)
 348 is slightly positive under some of the dry patches (Figure 2.g, day 16). [A similar high
 349 pressure anomaly in dry region has been found by Yang \(2018\)](#). A positive PSFC anomaly
 350 builds up a divergent flow at the surface, which exports low level moist air from the dry
 351 to the moist regions (figure 2.h). This flow further dries the dry regions which strengthen
 352 and expand. The divergent flow then increases the horizontal variance of water vapor

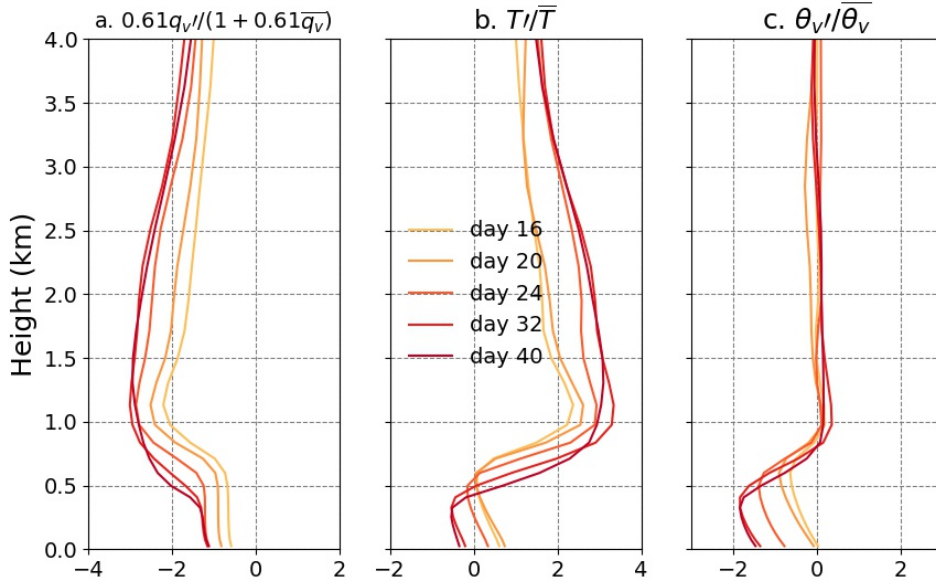


Figure 4. Plots show the contribution of a) q_v anomalies and b) temperature anomalies into c) virtual potential temperature anomalies. Each line is one day averaged over the dry patch ($CRH < 0.6$) for the simulation H5SST305.

353 which is correlated with the progress of aggregation. As mentioned in the introduction,
 354 this low-level divergent circulation and the concomitant up-gradient MSE transport are
 355 well documented in aggregation simulations (Bretherton et al., 2005; Muller & Held, 2012;
 356 Muller & Bony, 2015; Yang, 2018). Here we further investigate the origin of this high
 357 surface pressure anomaly in dry regions, and its link with specific humidity, radiation,
 358 and SST anomaly.

359 The horizontal gradients of virtual temperature are small in the free troposphere
 360 (Figure 4 and Figure 6.d) consistent with the weak temperature gradients of tropical re-
 361 gions where the Coriolis parameter is small (Sobel et al., 2001). Thus the surface pres-
 362 sure anomaly in dry regions is related to the boundary layer density anomaly. To deter-
 363 mine the depth of the boundary layer for each grid we find the height at which the gra-
 364 dient of specific humidity has its largest change. Using this definition, we see that the
 365 boundary layer height is uniform at the beginning of the simulation when moisture is
 366 uniformly distributed. But with the progress of aggregation and further dryness of dry
 367 regions, the boundary layer height reduces significantly in dry regions compared to the
 368 moist region. However we did not find the change in boundary layer height to impact
 369 the surface pressure anomaly (not shown). Thus in the following discussion on the source
 370 of the surface pressure anomaly we neglect the impact of boundary layer height.

371 To compare the air density, we use virtual potential temperature (hereafter θ_v): moist-
 372 ening / warming the air reduces the air density thus increases θ_v . Assuming hydrostatic
 373 balance in dry region (where we don't have any convection or even shallow clouds), the
 374 surface pressure anomaly depends on the virtual temperature anomaly, itself a function
 375 of temperature and moisture anomalies. In fact, we interpret the surface pressure anomaly
 376 in the dry regions as being the consequence of SST anomalies and boundary layer ra-
 377 diative cooling anomalies there. This is motivated by earlier work showing the key role
 378 played by low-tropospheric radiation in self-aggregation (Muller & Bony, 2015), and by

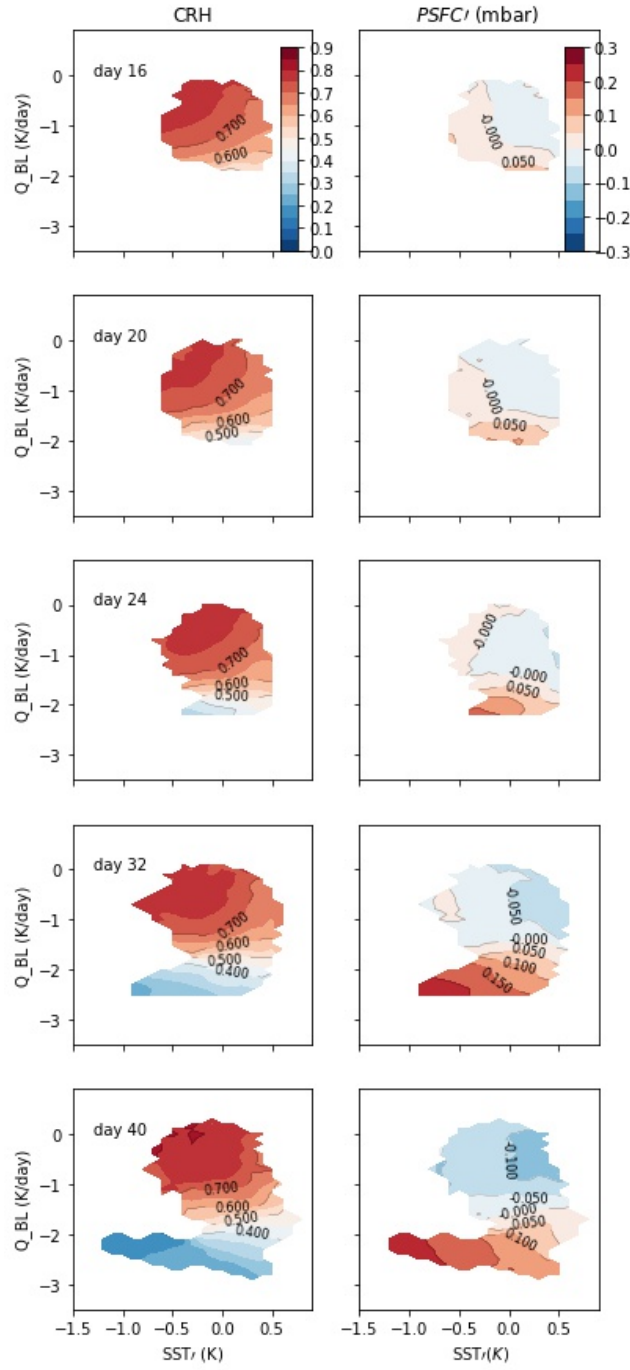


Figure 5. CRH (left column) and PSFC anomaly (right column) for simulation H5SST305. The x axis is SST anomaly, and the y axis is radiative cooling averaged over the boundary layer Q_{BL} . To compute the top of the boundary layer, we use the q_v profile and determine the first altitude above ground where it has a maximum curvature.

379 the theoretical model of Naumann et al. (2017, 2019) showing the similar or even larger
 380 radiatively driven shallow circulation compared to that driven by SST gradients. A lo-
 381 cally warmer SST tends to warm and moisten (through enhanced surface latent heat flux)
 382 the column and oppose the positive PSFC anomaly. On the other hand, a locally enhanced
 383 boundary layer radiative cooling (hereafter Q_{BL} , negative for a cooling) can cool and
 384 dry the boundary layer through subsidence, and generate a positive PSFC anomaly. In
 385 Appendix B, we confirm the key role played by locally enhanced boundary layer radi-
 386 ative cooling in sensitivity simulations: homogenizing it prevents the aggregation in our
 387 simulations, while homogenizing radiation in the free troposphere has little impact. Yang
 388 (2018) argued that locally enhanced boundary layer radiative cooling has a negative feed-
 389 back on the aggregation before and at the very early time of dry patch appearance and
 390 then turning to a positive feedback when the dry patches start growing. Here we argue
 391 that the boundary layer radiative cooling is necessary and creates a positive feedback
 392 from the beginning of dry patches appearance through its impact on the surface pres-
 393 sure anomaly. The difference between our results and (Yang, 2018) can be related to the
 394 fact that his feedback analysis (through the budget of vertically integrated available po-
 395 tential energy) only includes the direct diabatic effect of radiation, but does not take into
 396 account the indirect effect of the radiatively induced circulation and associated moisture
 397 transport.

398 From the early stage of the dry patch (day 16), the boundary layer moisture anomaly
 399 is negative and creates a negative θ_v anomaly (Figure 4.a); in other word, a positive pres-
 400 sure anomaly. The existence of a negative moisture anomaly and its positive contribu-
 401 tion to positive PSFC anomaly in dry region is consistent with the finding of Yang (2018).
 402 The temperature anomaly in dry patch is slightly positive at the beginning but then be-
 403 comes negative with further progress of the dry patch (Figure 4.b). So, up to day 20,
 404 the temperature profile of the boundary layer opposes the formation of a positive PSFC
 405 anomaly but after turning negative, it favors the positive PSFC anomaly, consistent with
 406 the SST anomaly discussed in the previous section, first positive opposing and second
 407 negative favoring aggregation.

408 Figure 5 shows the evolution of PSFC' in Q_{BL} and SST' space. At day 16, on the
 409 lower part of the panel (i.e. at more negative Q_{BL}), SST anomaly is positive thus warm-
 410 ing the column while Q_{BL} is large and cooling the column. Figure 4.b shows that the
 411 temperature anomaly of the dry region is still opposing the positive PSFC anomaly. But
 412 this opposition has been reduced by boundary layer radiative cooling. Indeed, the cool-
 413 ing generates subsidence (not shown), yielding a drying and concomitant moisture ef-
 414 fect on θ_v , which dominate the temperature effects and lead to the formation of a pos-
 415 itive PSFC anomaly (Figure 4.a).

416 As Figure 4 shows, the opposite effects of q_v and T on θ_v , up to day 20, might ex-
 417 plain why some of the dry patches do not persist at early stage and disappear. This op-
 418 posing impact results in a small θ_v anomaly thus small PSFC anomaly that has a low
 419 chance of persistence. By day 24, the center of the dry patch has a cold SST anomaly
 420 (§ 3.2), furthermore, Q_{BL} is enhanced as the column is drier (Figure 5). Thus the tem-
 421 perature of boundary layer also favors positive PSFC anomaly, so that PSFC anomaly
 422 shows a significant enhancement (Figure 2.g and 5).

423 The high pressure in dry region results in divergence and further expansion of dry
 424 patches. The dry patches are cloud free, even in the early warm stage. More precisely,
 425 convection stays outside the warm water and there is not any significant enhancement
 426 of convective activity at the edge of the dry patches with warm surface (S1). The stud-
 427 ies on the impact of SST gradient on convective activities (e.g. Liu & Moncrieff, 2008)

428 find an enhancement of rainfall where SST gradient is larger. This is due to a conver-
 429 gent flow induced by SST gradient. In our simulations, the regions of warm SST anom-
 430 alies are divergent and dry thus no convection or shallow cloud forms. In equilibrium state,
 431 when aggregation is fully reached, the surface under the convective area becomes cold
 432 thus the surface is divided into three regions: a cold and very dry, a warm and dry, and
 433 a moist and cold convective region. The moist convective region though does not move
 434 toward the warm anomaly and stays confined and motionless. Note that this is at odds
 435 with GCM studies of aggregation with interactive SST (Grabowski, 2006; Coppin & Bony,
 436 2017), where the moist patch always follows the warm SST anomaly which forms under
 437 the dry patch: a “cat and mouse” dynamics. In our cloud-resolving simulations, this mi-
 438 gration is absent as the dry patches have a persistent positive PSFC anomaly, which ex-
 439 tends even over its edge with warm SST anomaly. We interpret this discrepancy as re-
 440 sulting from a strong sensitivity of convection to local SST in GCMs. In our simulations,
 441 the enhanced boundary layer cooling by Q_{BL} compensates the warming by positive SST
 442 anomaly, thus along with a negative boundary layer moisture anomaly creates a posi-
 443 tive PSFC anomaly. So higher pressure remains located over the dry regions, and con-
 444 vection remains localized in moist regions.

445 The picture that emerges is that enhanced boundary layer radiative cooling in dry
 446 regions dries the boundary layer and thus through virtual effects creates a high pressure
 447 anomaly there. This positive PSFC anomaly is partially offset by warmer SSTs at early
 448 stages of the aggregation process. Once the dry patch is dry enough, the SST anomaly
 449 reverses because of enhanced surface cooling by longwave radiation and the colder SST
 450 adds to the boundary layer cooling in dry regions, and by hydrostasy to positive PSFC
 451 anomaly. The sign and magnitude of PSFC anomaly has a large impact on the persis-
 452 tence and growth of dry patches. More precisely, a positive PSFC anomaly ensures the
 453 expansion of dry patches by exporting moist static energy via a boundary layer diver-
 454 gent flow out of dry patches. As this divergent flow is found to be crucial for the speed
 455 of aggregation, we explore it in more detail in the following section.

456 3.4 Divergent flow

457 The surface wind is divergent in dry patches from their early stage (Figure 2.h).
 458 From earlier studies on aggregation, it is known that this low-level divergent circulation
 459 is key in transporting moisture and MSE out of dry patches, strengthening moisture and
 460 MSE gradients. The dry patches then expand (e.g., (Bretherton et al., 2005)). Consis-
 461 tent with the theoretical model of (Naumann et al., 2017), we saw that this low-level cir-
 462 culation can be related to the persistence of a high surface pressure anomaly, itself re-
 463 lated to negative moisture anomaly, stronger boundary layer cooling, and SST anomaly.
 464 Here we investigate further the vertical structure of this circulation. Figure 6 shows a
 465 vertical cross section of winds, pressure, potential temperature (θ) and virtual potential
 466 temperature (θ_v) anomalies at day 32. We see that the divergent flow is indeed located
 467 in the boundary layer (below 1 km or so, see Figure 6.c) where θ_v has a large variance
 468 (Figure 6.e). In the free troposphere, consistent with theoretical expectations in the trop-
 469 ics (Sobel et al., 2001), θ_v anomalies are small.

470 The divergent flow can also be shown using the stream function (Ψ) in CRH - height
 471 space (Bretherton et al., 2005):

$$\Psi_i(z) = \Psi_{i-1}(z) + \sum_{CRH \in [CRH_{i-1}, CRH_i]} \overline{\rho(z)} w(z), \quad (7)$$

472 where i is the index of CRH bin (sorted), w is the vertical velocity summed in the CRH
 473 bin i , $\bar{\rho}$ is the domain-mean density profile, and $\Psi_0 = 0$ for all z . This stream function

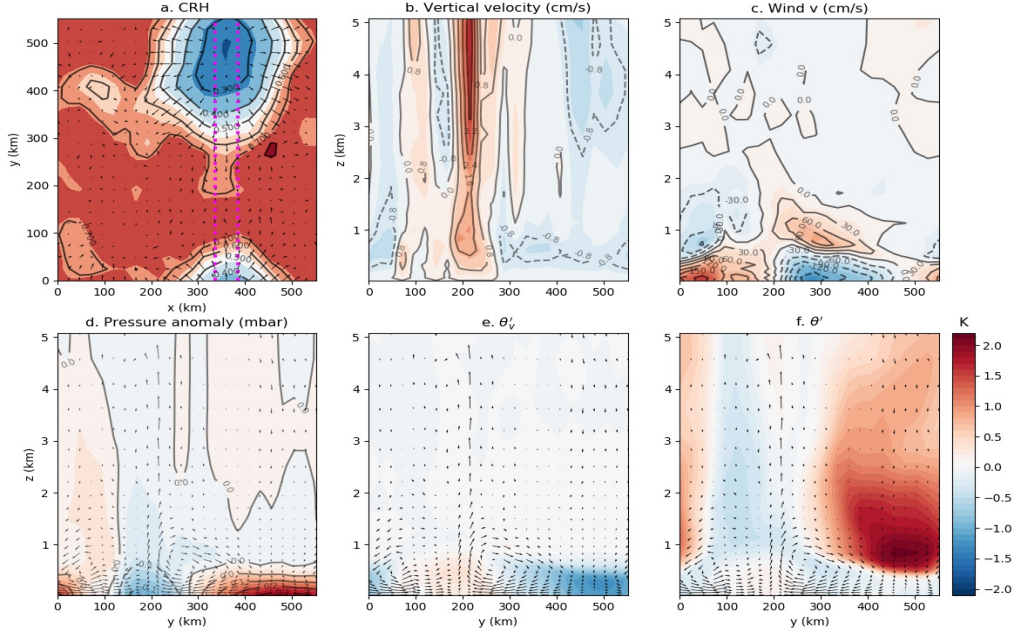


Figure 6. Simulation H5SST305, (a) shows the top view of CRH at day 32. (b)-(e) are the vertical profile between magenta line in panel (a) averaged in x direction. The dry patch is centered around $y = 500$ km. (b) and (c) shows respectively the vertical profile of vertical and horizontal velocity. (d), (e), and (f) shows respectively pressure anomaly (mbar), θ_v anomaly and θ anomaly. Colorbar corresponds to panels (e) and (f).

474 represents the total mass transport between low and high CRH bins. Figure 7 shows that
 475 it has one maximum below 3 km (which we refer to as the boundary layer divergence)
 476 and one maximum in the free troposphere (which we refer to as the deep circulation).
 477 The boundary layer divergence extends from dry to moist regions where the PSFC gra-
 478 dient is maximum, consistent with the boundary layer divergence of the snapshot shown
 479 in Figure 6.

480 Indeed, the maximum of the stream function Ψ at low levels is exactly equal to the
 481 boundary layer divergence out of dry regions and into moist regions:

$$\Psi_{max} = \int_0^{z_{max}} \rho u_{max} dz, \quad (8)$$

482 where z_{max} denotes the height of the stream function maximum, and ρu_{max} is the to-
 483 tal mass transport through the CRH bin of the stream function maximum (about 0.65
 484 on Figure 7), i.e. total mass transport from low CRH to high CRH values.

485 As figure 6 and figure 7 show, part of the boundary layer divergence returns to the
 486 dry region higher in the boundary layer (around ≈ 2 km), while the rest of it is trans-
 487 ported upward. Here we define the shallow circulation as part of the flux that stays in
 488 the boundary layer (circulation below 4 km or so). It is given by $\Psi_{max} - \Psi_{min}$, where
 489 Ψ_{min} is the minimum of the streamfunction (around 4 km). It is this shallow circula-
 490 tion which exports low-level air with high MSE from dry regions, and imports air with
 491 low MSE at the top of the boundary layer into dry regions, i.e. up-gradient. This shal-
 492 low circulation thus has negative gross moist stability, leading to aggregation, e.g. Neelin
 493 and Held (1987); Bretherton et al. (2005); Raymond et al. (2009).

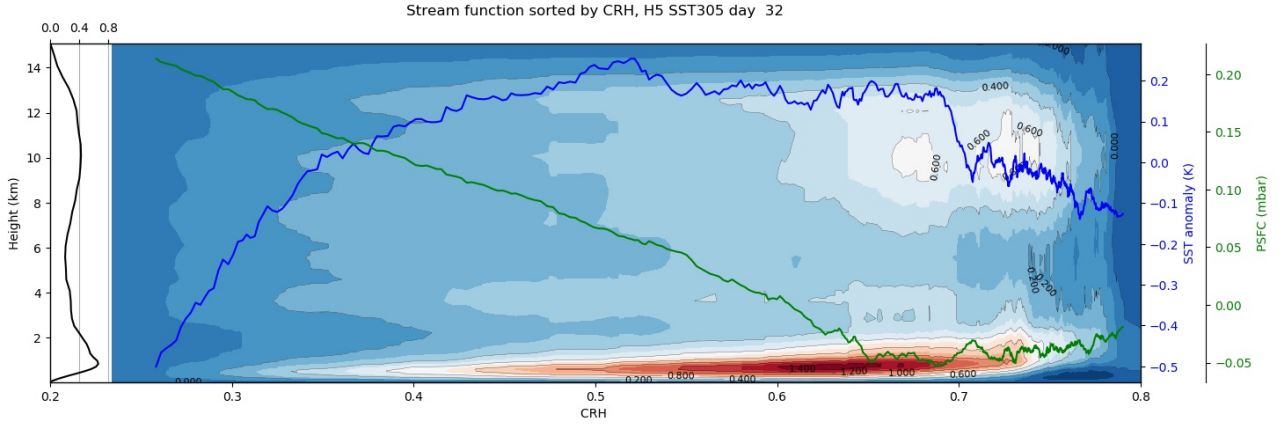


Figure 7. Stream function for simulation H5SST305 at day 32 (color and contours, $Kg.m^{-2}.s^{-1}$). Black line on the left side of the panel shows the stream function averaged over the domain. Blue line shows the SST anomaly and green line shows PSFC anomaly both sorted by CRH.

494 The deep circulation on the other hand (which is given by $\Psi_{max,deep}$ secondary stream-
 495 function maximum around 10 km) disfavors aggregation by transporting air with high
 496 MSE (found at high altitudes, above 10 km on Figure 7) out of the moist convective re-
 497 gion, thus down-gradient (positive gross moist stability). Therefore, the more bottom
 498 heavy the circulation, the more favored the aggregation. We further explore the role of
 499 this shallow circulation, and the importance of the ratio of shallow to deep circulation
 500 on the speed of aggregation, in the following section, where we extend our study to var-
 501 ious slab ocean depths and mean SSTs.

502 4 The impact of slab depth and SST on self-aggregation

503 4.1 Delayed aggregation with shallow mixed layer and cold SST

504 To investigate the impact of slab depth and domain mean SST on our findings, we
 505 extend the analysis of § 3 to two more depths of the slab, $H=10$ and 50 meters, and one
 506 more domain mean surface temperature $SST_0 = 300$ K. As was shown earlier (figure
 507 1 and § 3.1), introducing an interactive SST typically slows down the aggregation, and
 508 the delay obtained (tens of days) is comparable to the delay due to decreasing the mean
 509 SST in fixed SST simulations (from 305 K to 300 K). Based on the aggregation index
 510 (figure 1), we define two regimes: **Regime 1 when the aggregation index increases slowly.**
 511 **We refer to this period as Latency.** And regime 2 with monotonic and fast increase of
 512 the aggregation index to its maximum value. We refer to this period as Transient. In
 513 the following we elaborate on the impact of slab depth and domain mean sea-surface tem-
 514 perature on each of these periods.

515 a. Latency

516 Figure 8 shows the relative contributions of SST anomaly and boundary layer cool-
 517 ing in dry regions in the different simulations. We see that with a shallower mixed layer
 518 depth, the warm SST anomaly in dry regions is larger and persists longer than with a

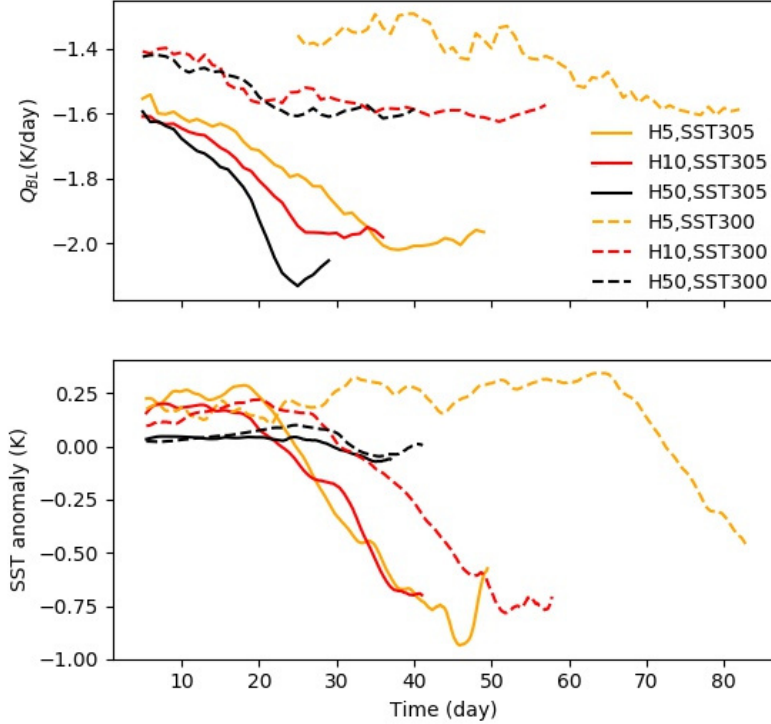


Figure 8. Time series of (top) Boundary layer radiative cooling anomaly (difference between dry and moist region), and (bottom) surface temperature anomaly averaged over the dry patch.

519 deeper mixed layer. Thus with a shallower slab, the probability that a dry patch, at its
 520 first stage, recovers its moisture and disappears, is larger. This process can significantly
 521 delay the aggregation or potentially prevent it if the warm anomalies are large enough.
 522 Otherwise, if the negative feedback by SST is not as strong as positive feedback by ra-
 523 diative cooling, the aggregation index increases but slowly. For example, the aggrega-
 524 tion indices in the simulations H5SST300 and H10SST300 have respectively the latency
 525 equal to 70 and 35 days. Thus the larger the warm SST anomalies (or the shallower the
 526 slab), the longer the latency. As Figure 1 shows, when the slab depth is large (especially
 527 at 305 K), the latency goes to zero. As expected, the deepest slab are close to simula-
 528 tions with fixed SST.

529 We also find that for a given slab depth, the latency is longer at 300 K compared
 530 to 305 K. Specifically, the latency for H5SST305 is about 30 days while for H5SST300
 531 it is around 70 days. We interpret this longer latency as being the result of the signif-
 532 icantly weaker Q_{BL} at 300 K (Figure 8), while SST anomalies have similar magnitudes.
 533 Weaker Q_{BL} has a smaller contribution to the high pressure PSFC, so the negative feed-
 534 back from SST anomaly become more important, leading to a longer latency.

535 The reason why Q_{BL} is smaller at 300 K is not clear, however, it could be related
 536 to the specific humidity of the free troposphere. At 305 K, the free tropospheric specific
 537 humidity is larger (due to the thermodynamic constraint given by the Clausius-Clapeyron
 538 equation, which predicts an approximately exponential increase of specific humidity with
 539 temperature for constant relative humidity). Consequently, the decrease of specific hu-
 540 midity due to subsidence in dry regions, which is proportional to the specific humidity,

541 is more rapid at 305 K compared to 300 K. The free tropospheric dryness allows the bound-
 542 ary layer to radiatively cool more efficiently and have a stronger contribution to PSFC.
 543 We will come back to this large scale circulation in § 4.2.

544 In summary, the longer latency at shallower slabs can be understood by the warmer
 545 SST anomaly in dry regions (Figure 8.b), leading to reduced surface pressure and thus
 546 reduced boundary layer divergence (Figure 9 .a). But the SST anomaly is very similar
 547 at cold (300) and warm (305) SST, at least at early times. Thus the longer latency at
 548 colder SSTs is instead due to weaker boundary layer cooling (Figure 8.a), reducing the
 549 radiatively-driven divergence.

550 b. Transient

551 During the transient period, the aggregation index (Figure 1) monotonically increases
 552 to reach its maximum. As we will see here, the slope of the index evolution, which de-
 553 termines the timing of the aggregation, depends on the strength of the shallow circula-
 554 tion and associated up-gradient transport of MSE, itself function of Q_{BL} and *SST* anoma-
 555 lies.

556 Figure 8 shows that, after the latency period, both stronger radiative cooling and
 557 colder SST anomalies contribute to the high surface pressure in dry regions. The largest
 558 change comes from the SST anomaly, which drops sharply in the H10 and H5 simula-
 559 tions (Figure 8.b); the increase in radiative cooling is more gradual and stronger in the
 560 305 K simulations. Once these two cooling effects both contribute to higher surface pres-
 561 sure, aggregation progresses faster, consistent with the increase in the aggregation in-
 562 dex (Figure 1).

563 Thus, with interactive SST, the SST anomalies have an opposition - acceleration
 564 impact on the shallow circulation. The early warm anomaly in dry regions opposes the
 565 virtually- and radiatively-driven divergent flow and concomitant export of MSE, thus
 566 opposing the aggregation; but the later cold anomaly in dry regions reinforces the di-
 567 vergent flow, thus reinforcing the aggregation.

568 This is well captured in Figure 9.a, which shows the strength of the shallow circula-
 569 tion ($\Psi_{max} - \Psi_{min}$, see § 3.4) in the various simulations. For the shallower slabs, the
 570 shallow circulation has a fairly constant value at the beginning (latency regime) followed
 571 by a rapid monotonic increase, while for deeper slabs, the SST anomalies are very small
 572 so the ‘opposition-acceleration’ impact is absent and the shallow circulation has a mono-
 573 tonic increase from the beginning. The deep circulation on the other hand (Figure 9.b)
 574 does not show a strong dependence on slab depth or on SST.

575 These results suggest that the aggregation speed is determined by the shallow cir-
 576 culation between dry and moist regions. Figure 9.b also suggests that the deep circu-
 577 lation is not directly linked to the aggregation speed, though we note that the free-tropospheric
 578 drying (Figure 3), which strongly affects the boundary layer cooling and thus the shal-
 579 low circulation, is closely related to the deep circulation. Although not directly linked
 580 to the dry region strengthening and expansion, the deep circulation could therefore play
 581 a role in the onset of aggregation, through its impact on boundary layer radiation. We
 582 explore this in more detail in the next section.

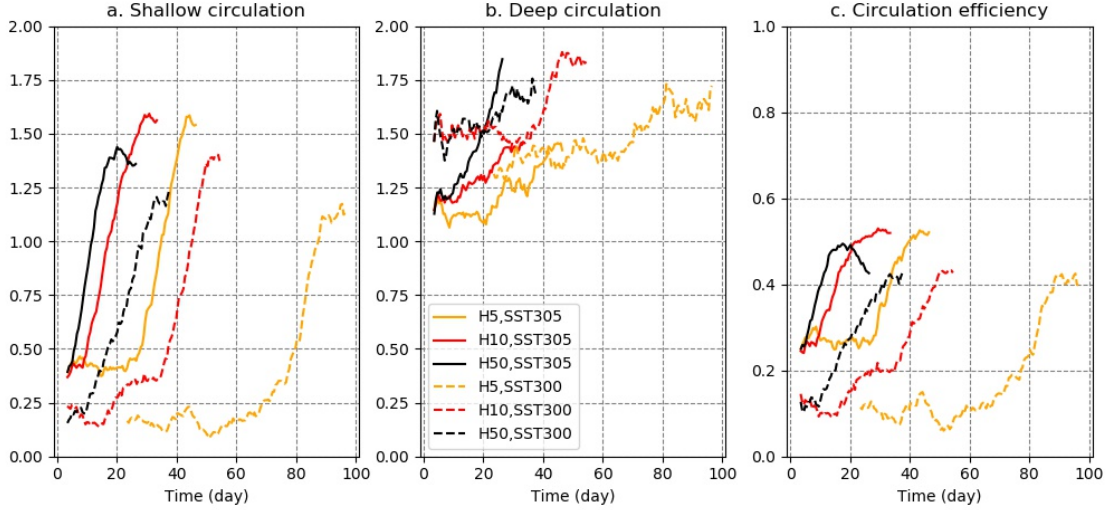


Figure 9. Time evolution of the (a) shallow, (b) deep circulation strength and (c) the circulation efficiency η . Plots are smoothed using a running mean with a 7 day window.

583
584

4.2 Link with the strength of the shallow circulation compared to the deep circulation

585
586
587
588
589

The vertical structure of the streamfunction (Figure 7) shows two cells: a shallow circulation with a maximum below 3 km or so, and a deeper cell with a maximum around 10 km or so. As noted earlier §3.4, the shallow circulation is given by $\Psi_{max} - \Psi_{min}$ and is associated with the boundary layer divergence out of the dry column, which occurs below the height of the maximum.

590
591
592

To capture more accurately the shallow circulation, and its [relative contribution to the total circulation \(shallow plus deep which, as noted in § 3.4, is given by \$\Psi_{max,deep}\$ \)](#), we introduce a circulation efficiency η :

$$\eta = \frac{\Psi_{max} - \Psi_{min}}{\Psi_{max,deep} + \Psi_{max} - \Psi_{min}}. \quad (9)$$

593
594
595
596
597
598
599
600
601
602

The numerator is the fraction of boundary layer divergence out of dry regions into moist regions, which returns to the dry regions below the height of the minimum, 4 km or so. It thus indeed quantifies the shallow circulation. The denominator is the sum of this shallow circulation and of the deep circulation. The latter includes air that has converged into moist regions at low levels as well as in the free troposphere (between the minimum and the deep maximum), and returns to the dry regions above the height of the deep maximum, above 10 km or so. The denominator thus quantifies the overall large-scale circulation, measured by the total mass transport between dry and moist regions. So η (between 0 and 1) measures the fraction of mass transport between dry and moist regions which is done by the shallow circulation.

603
604
605
606

Figure 9.c shows the time evolution of the circulation efficiency in the various simulations. The link with the aggregation evolution is clear: the simulations with higher circulation efficiency have faster aggregation (Figure 1). This is consistent with earlier studies of self-aggregation, which highlight the key role played by the MSE transport of

607 the shallow circulation. From the previous section, the shallow circulation is driven by
 608 boundary layer radiative cooling and SST anomalies in dry regions, generating hydro-
 609 static high surface pressure anomalies through cooling and virtual effects.

610 As noted earlier, Figure 9.b suggests little contribution from the deep circulation.
 611 But larger Q_{BL} can occur in response to relatively drier upper free troposphere, itself
 612 connected to the efficiency of the deep circulation via subsidence drying. Thus, although
 613 the deep circulation has little contribution to the aggregation progress or dry region strength-
 614 ening, we can not rule out its contribution to the onset of aggregation and of dry regions.
 615 The subsidence drying in the free troposphere, which can be seen in Figure 3, could play
 616 an important role in initiating the boundary layer cooling enhancement in dry regions,
 617 which then amplifies the drying, high pressure and low-level divergence.

618 The deep circulation is determined by the upward mass transport in deep moist
 619 convection, and in our doubly-periodic domain by the compensating subsidence in cloud-
 620 free areas. The strength of the subsidence velocity in cloud-free areas can be quantified
 621 using the weak temperature gradient (WTG) approximation as follows:

$$w_{WTG} = \frac{Q_{rad}}{\Gamma}, \quad (10)$$

622 where

$$\Gamma = \frac{T}{\theta} \frac{d\theta}{dz} \quad (11)$$

623 is the stratification, Q_{rad} is the radiative cooling, T is temperature, and θ is potential
 624 temperature. Our findings show that (Figure 10) Q_{rad} in the dry region is larger at higher
 625 SST (Figure 10.b), but so is Γ (Figure 10.a), so that W_{WTG} does not explain the dif-
 626 ferent timings of aggregation between the two SSTs (Figure 10.c): for instance H5SST305
 627 and H5SST500 have approximately the same maximum W_{WTG} while their aggregation
 628 speed is very different (Figure 1; we note in passing that the maximum W has similar
 629 magnitude but occurs higher in the warmer simulation, consistent with theoretical ex-
 630 pectations (Singh & O’Gorman, 2012)).

631 But enhanced drying is still expected from subsidence, as it is given by $W_{WTG} \partial q_v / \partial z$,
 632 and the gradient of specific humidity $\partial q_v / \partial z$ is larger at warmer SSTs (Figure 10.d). In
 633 the subsiding regions, the free tropospheric drying is thus expected to be stronger at warmer
 634 SST, enhancing the boundary layer cooling and the radiatively-driven divergence. We
 635 suggest that the positive PSFC anomaly in the dry region is the organizer of the con-
 636 vective clouds by exporting low level moist air from the dry patches and expanding them.
 637 But the formation of a positive PSFC anomaly is a response to the large-scale deep cir-
 638 culation and free-tropospheric drying, and is necessary for the persistence and expan-
 639 sion of dry patches leading to the confinement of convection.

640 5 Conclusions

641 The importance of sea surface temperature on the aggregation of convective clouds
 642 has been shown in earlier studies, however mostly using a constant and uniform SST (e.g.,
 643 Wing, 2019). Here we study the feedbacks between an interactive SST and the aggre-
 644 gation of convective clouds using a 3D RCE setup. To have an interactive surface tem-
 645 perature, we use an slab ocean with fixed mean SST but locally varying temperature.

646 Consistent with earlier studies, we find that the presence of an interactive SST de-
 647 lays the aggregation of convection, and the stronger the interaction (smaller slab depth)

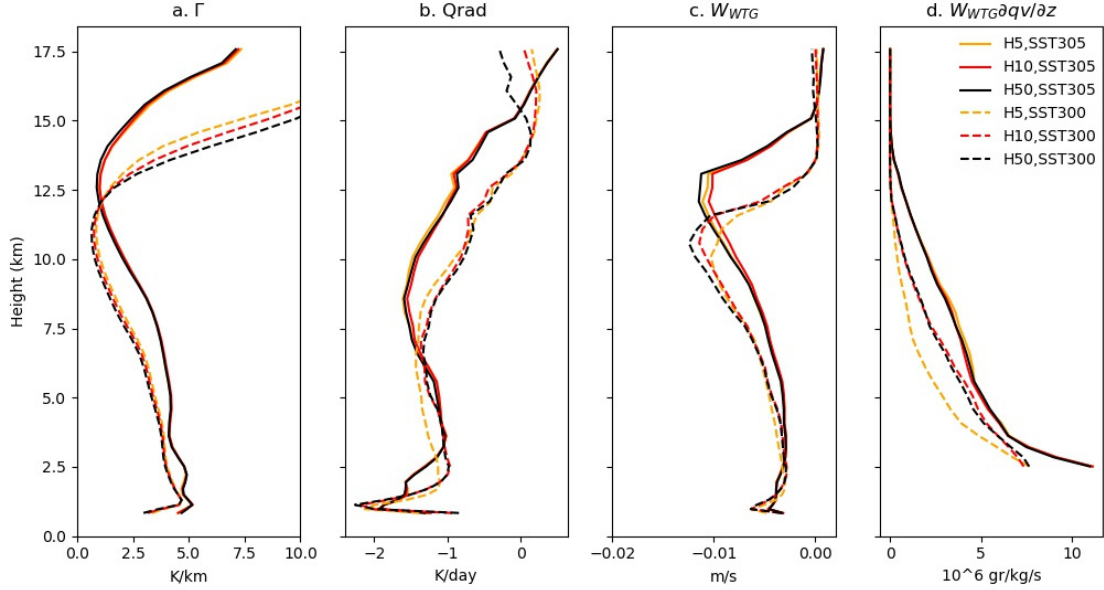


Figure 10. Plot shows: a) the stratification, b) atmospheric radiative cooling, c) vertical velocity computed by WTG, and d) dryness tendency. The variables are averaged over transient part ($0.2 < \delta CRH < 0.5$ in Figure 1)

648 the longer the delay. It has been suggested (Hohenegger & Stevens, 2016) that this delay
 649 could be due to the development of an SST gradient between dry and moist regions,
 650 with a warm anomaly in dry regions opposing the shallow circulation believed to play
 651 a crucial role in the aggregation process. Indeed, the onset of aggregation, and the as-
 652 sociated strengthening and expansion of dry regions, is associated with a shallow circula-
 653 tion (below 4 km or so). This shallow circulation diverges from dry regions near the
 654 surface and in the boundary layer, and returns back into dry regions just above the bound-
 655 ary layer. It thus transport MSE from dry into moist regions, i.e. up-gradient, and has
 656 negative gross moist stability, reinforcing MSE gradients and leading to aggregation (Bretherton
 657 et al., 2005; Muller & Held, 2012).

658 We find that the surface temperature anomaly underneath the dry patches actu-
 659 ally depends on their dryness. At first, the dryness is small, and warming by shortwave
 660 radiation dominates the cooling by latent heat flux and surface longwave radiation, so
 661 that the surface under the dry patch warms. But when the dryness becomes large, the
 662 surface can cool more efficiently due to predominantly enhanced surface longwave radi-
 663 ative cooling as the column is dry and downward longwave radiation reduces (the dry-
 664 ness also results in the enhancement of LHF though it is small compared to longwave
 665 radiative cooling).

666 This first positive and then negative SST anomaly in dry regions has an impact
 667 on the surface pressure anomaly in dry regions, which is important for driving the afore-
 668 mentioned shallow circulation and guaranteeing the growth and expansion of the dry patch.
 669 When positive, the SST anomaly under the dry patch opposes the divergent boundary
 670 layer flow out of the dry patch, while if negative it adds to the positive PSFC anomaly
 671 and further helps the divergent flow and concomitant expansion of the dry patch. How-
 672 ever, even with an initially positive SST anomaly, the dry patch has a positive PSFC,
 673 due to enhanced boundary layer radiative cooling. This radiative cooling decreases the

674 boundary layer temperature and humidity via subsidence drying, resulting in higher PSFC
 675 (by virtual effects). Then, when the SST anomaly becomes negative, it adds to the high
 676 PSFC anomaly and thus enhances the divergent flow from dry regions and the aggre-
 677 gation. So the SST anomaly has an opposition - acceleration impact on aggregation, and
 678 the differential boundary layer radiative cooling and virtual effects are necessary for trig-
 679 gering the aggregation.

680 In the Earth's tropics, the surface temperature in clear-sky areas is usually warmer
 681 than the surrounding as a result of enhanced shortwave radiation at the surface, broadly
 682 corresponding to the initial warming discussed above. The second cooling phase discussed
 683 above, which occurs after tens of days, requires a dry atmosphere. In our simulation at
 684 300 K, when the precipitable water at the center of the dry patch reaches below about
 685 15 mm (corresponds to CRH \approx 0.4) the net surface radiation can have a cooling effect.
 686 Using ERA5 reanalysis, we find that over the tropics, PW \leq 15 mm is not rare. How-
 687 ever, the cooling effect is a slow process and its time scale depends on the depth of ocean
 688 mixed layer. In our CRM simulations with double periodicity, the dry patches are per-
 689 sistent enough for the surface cooling by radiation to become important. Whether this
 690 can be the case over the tropics deserves further investigation.

691 We note that although the PSFC anomalies originate from boundary layer virtual
 692 temperature anomalies, they are the result of the response of the boundary layer to the
 693 free tropospheric moisture reduction. It is indeed the free-tropospheric drying which al-
 694 lows larger boundary layer radiative cooling and injection of free tropospheric dry air
 695 into the boundary layer. The PSFC anomaly is thus the organizer of convection, or the
 696 amplifier of aggregation, by creating the shallow circulation which transports low-level
 697 air with high MSE up-gradient and favors aggregation. But the free-tropospheric dry-
 698 ing appears to be initiating the process. A circulation efficiency, which measures the strength
 699 of the shallow circulation relative to the overall circulation (shallow + deep), is found
 700 to correlate well with the speed of aggregation. Interestingly, the shallow circulation strength
 701 increases strongly in the simulations as aggregation proceeds, while the deep circulation
 702 remains much more constant. When the SST anomaly in the dry patch turns negative,
 703 the shallow circulation shows a clear strengthening due to the increased high PSFC anomaly.

704 Using different slab depths and SSTs, our findings confirm that the aggregation is
 705 faster with deeper slab and at higher SST. When the slab is shallow, warm SST anom-
 706 alies that form at the early stage of dry patches weakens the pressure anomalies thus the
 707 shallow circulation. This weakening delays the aggregation. We also find that at higher
 708 SST, the boundary layer radiative cooling is larger for the same dryness, so that the neg-
 709 ative impact of the warm SST anomaly on PSFC is less important compared to the pos-
 710 itive impact of the stronger boundary layer radiative cooling.

711 The initial free-tropospheric drying is also found to be sensitive to SST. The free
 712 tropospheric radiative cooling is stronger at higher SST (but largely independent of slab
 713 depth for a given SST). However, the atmospheric stratification is also larger at higher
 714 SST so that the free-tropospheric subsidence velocity calculated using the WTG approx-
 715 imation (Sobel et al., 2001) does not explain the different speeds of aggregation in our
 716 simulations. But the resulting free-tropospheric moisture tendency is larger at higher SST.
 717 Larger free-tropospheric drying at warmer SST yields enhanced boundary layer radia-
 718 tive cooling, itself leading to the formation of positive PSFC anomalies. Therefore the
 719 boundary layer shallow circulation determines the speed of aggregation, but the deep cir-
 720 culation, and the associated free-tropospheric drying, appear to be necessary for the for-
 721 mation of a high surface pressure anomaly in dry regions leading to the shallow cir-
 722 culation.

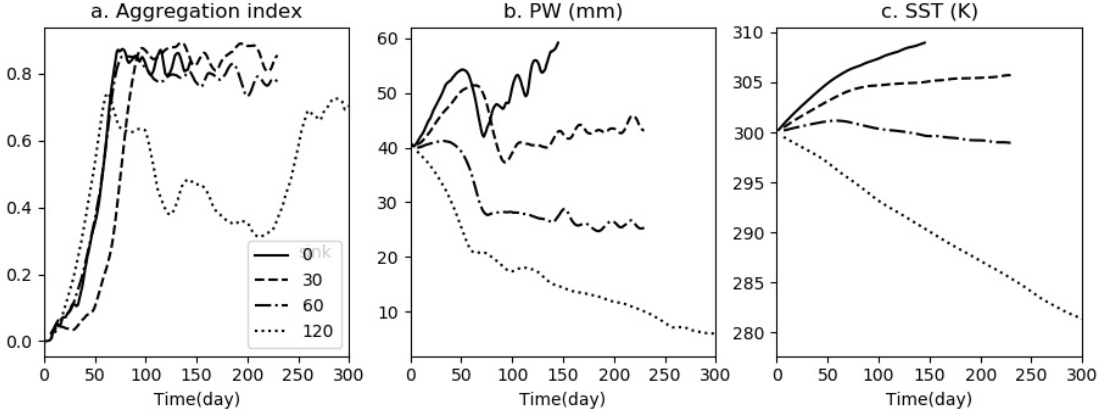


Figure A1. Time evolution of a. aggregation index, b. PW, and c. domain mean surface temperature for simulations with constant sink equal to 0 W/m² (solid line), 30 W/m² (dashed line), 60 W/m² (dashed dotted line), and 120 W/m² (dotted line).

Appendix A Impact of interactive SST with constant deep ocean sink

As mentioned in § 2.3, the incoming solar flux in the tropics exceeds the threshold for runaway greenhouse warming (Pierrehumbert, 2010). As a consequence, in closed domain simulations with interactive SST such as those used here, without the oceanic and atmospheric transport of energy out of the tropics, the SST increases without bound (Hohenegger & Stevens, 2016). Relaxing the domain mean SST to a target SST, as is done in this study, allows to prevent this runaway greenhouse warming, and maintains the domain mean SST close to constant.

Another possibility to avoid the runaway greenhouse warming is to add a sink of energy, e.g. into the deep ocean (following (Romps, 2011)). Figure A1 shows the time evolution of the aggregation index, domain-mean PW, and domain-mean SST for simulations where a spatially and temporally constant ocean sink of energy of varying strength (from 0 to 120 W m⁻²) is added to the surface energy budget (negative term added to the right-hand side of equation 2 instead of the relaxation term on the left-hand side). The slab depth is 10 meters and the initial temperature is 300 K for all simulations. In order to investigate the sensitivity to the amount of sink, four different sinks of energy are tested: 0, 30, 60, and 120 W m⁻².

For all 4 sinks, the aggregation proceeds. For sink = 0 W m⁻², as expected, the domain-mean SST increases quickly. The aggregation reduces the increasing trend of SST (as aggregation is associated with increased Outgoing Longwave Radiation, or OLR, cooling, e.g. (Wing & Emanuel, 2014)) but does not stop it, as the amount of energy reaching the surface is still large and it is thus not in equilibrium energetically. PW shows a sharp reduction with aggregation but with surface warming, it continues increasing. For sink = 30 W m⁻², the domain mean SST has a very modest increase after aggregation as the sink of energy is very close to the surface energy imbalance when aggregated (40 W/m²). The simulation with sink = 60 W/m² starts cooling after aggregation but does not disaggregate with cooling (not shown) as the aggregation is favored even at cold SST = 295 K in our simulations (Shamekh et al., 2019).

751 When the energy sink is large, equal to 120 W m^{-2} , the surface cools strongly and
 752 the cooling is enhanced by aggregation. Interestingly, this simulation disaggregates partially
 753 around $\text{SST} = 295 \text{ K}$ and day 50, but aggregates again when the SST drops below
 754 285 K around day 220. The disaggregation - re-aggregation be seen easily in Figure
 755 A1.a.

756 It has been as was hypothesized in past studies (e.g. Khairoutdinov & Emanuel,
 757 2010) that self-aggregation could be a way for tropical temperatures to regulate themselves
 758 . Indeed, since aggregation is associated with increased OLR, it was suggested that
 759 as SST increases, self-aggregation is favored, yielding more OLR cooling and reducing
 760 the SST back towards its initial value. So maybe the tropical atmosphere could "regulate"
 761 its temperature through modulation of its convective aggregation. However, the
 762 oscillation between aggregation - disaggregation does not happen in our simulations (or
 763 it is very sensitive to the ocean sink), as the aggregation is favored over a large range
 764 of SST.

765 In summary, independent of the sink, all the simulations aggregate. But the final
 766 SST and PW of the simulations depend on the sink of energy. In order to minimize drift
 767 in domain mean SST, and also to avoid the sensitivity of results to the strength of the
 768 imposed ocean sink, in this study we instead avoid the runaway greenhouse climate by
 769 relaxing the domain mean SST towards a target temperature.

770 Appendix B Sensitivity simulations and low-level radiative cooling

771 In order to verify the importance of boundary layer radiative cooling, we run 3 sen-
 772 sitivity tests by homogenizing the radiative cooling profile at: 1. all levels (mentioned
 773 as homrad in Figure B1, 2. in the boundary layer which we crudely define to be up to
 774 1 km above the surface (referred to as BL-homrad), and 3. in free troposphere, above
 775 1 km to the top of the domain (mentioned as FT-homrad).

776 As figure B1 shows for both temperatures, 300 and 305 K, radiative cooling feed-
 777 backs are necessary for self-aggregation so that homogenizing the radiation profile pre-
 778 vents the self-aggregation. The results also show that for FT-homrad, in which the ra-
 779 diation is homogenized only in free troposphere, the aggregation proceeds without sig-
 780 nificant difference from the control simulations (fullrad). But homogenizing the bound-
 781 ary layer radiative feedback (BL-homrad in Figure B1) prevents the aggregation. These
 782 findings are consistent with Bretherton et al. (2005) who emphasize the role of low-tropospheric
 783 / boundary layer radiative cooling, as well as with Muller and Held (2012) who find the
 784 shallow clouds radiative feedbacks to be important for the aggregation onset.

785 Acknowledgments

786 This project has received funding from the Marie - Sklodowska Curie Actions (MSCA)
 787 under the European Union's Horizon 2020 research and innovation programme (grant
 788 agreement No. 675675). CJM gratefully acknowledges funding from the European Re-
 789 search Council (ERC) under the European Union's Horizon 2020 research and innova-
 790 tion programme (Project CLUSTER, grant agreement No. 805041). The authors also
 791 thank Grand Équipement National De Calcul Intensif (GENCI), France, for providing
 792 access and support to their computing platforms Très Grand Centre de Calcul (TGCC).
 793 Data used in this study will be available at <https://figshare.com>

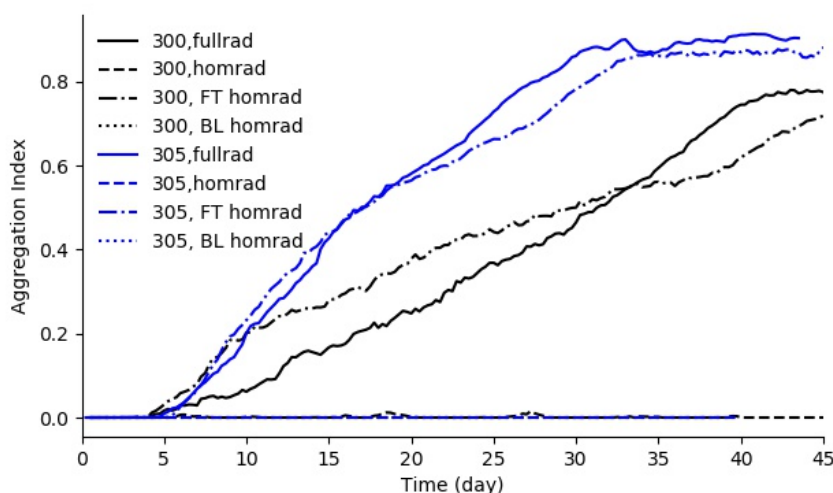


Figure B1. Plot shows the aggregation index time series for the sensitivity tests at 300K (black curves) and 305 K (blue curves). Homrad, FT and BL stand for homogenized radiation, free troposphere and boundary layer respectively.

794

References

- 795 Arnold, N. P., & Randall, D. A. (2015). Global-scale convective aggrega-
 796 tion: Implications for the madden-julian oscillation. *Journal of Advances*
 797 *in Modeling Earth Systems*, 7(4), 1499-1518. Retrieved from [https://](https://agupubs.onlinelibrary.wiley.com/doi/abs/10.1002/2015MS000498)
 798 agupubs.onlinelibrary.wiley.com/doi/abs/10.1002/2015MS000498 doi:
 799 10.1002/2015MS000498
- 800 Back, L. E., & Bretherton, C. S. (2009). On the relationship between sst gradi-
 801 ents, boundary layer winds, and convergence over the tropical oceans. *Journal*
 802 *of Climate*, 22(15), 4182-4196. Retrieved from [https://doi.org/10.1175/](https://doi.org/10.1175/2009JCLI2392.1)
 803 [2009JCLI2392.1](https://doi.org/10.1175/2009JCLI2392.1) doi: 10.1175/2009JCLI2392.1
- 804 Bretherton, C. S., Blossey, P. N., & Khairoutdinov, M. (2005). An energy-balance
 805 analysis of deep convective self-aggregation above uniform SST. *J. Atmos. Sci.*,
 806 62(12), 4273-4292. doi: 10.1175/JAS3614.1
- 807 Collins, W. D., Rasch, P. J., Boville, B. A., Hack, J. J., McCaa, J. R., Williamson,
 808 D. L., ... Zhang, M. (2006). The formulation and atmospheric simulation
 809 of the community atmosphere model version 3 (cam3). *J. Climate*, 19(11),
 810 2144-2161. doi: 10.1175/JCLI3760.1
- 811 Coppin, D., & Bony, S. (2015). Physical mechanisms controlling the initiation of
 812 convective self-aggregation in a general circulation model. *J. Adv. Model.*
 813 *Earth Syst.*, 7(4), 2060-2078. doi: 10.1002/2015MS000571
- 814 Coppin, D., & Bony, S. (2017). Internal variability in a coupled general circulation
 815 model in radiative-convective equilibrium. *Geophys. Res. Lett.*, 44(10), 5142-
 816 5149.
- 817 Coppin, D., & Bony, S. (2018). On the interplay between convective aggregation,
 818 surface temperature gradients, and climate sensitivity. *Journal of Advances in*
 819 *Modeling Earth Systems*, 10(12), 3123-3138. doi: 10.1029/2018MS001406
- 820 Craig, G. C., & Mack, J. M. (2013). A coarsening model for self-organization of
 821 tropical convection. *J. Geophys. Res.*, 118(16), 8761-8769.
- 822 Cronin, T. W., Emanuel, K. A., & Molnar, P. (2015). Island precipitation enhance-

- 823 ment and the diurnal cycle in radiative-convective equilibrium. *Quart. J. Roy.*
824 *Meteor. Soc.*, *141*(689), 1017–1034.
- 825 Emanuel, K. A., Wing, A. A., & Vincent, E. M. (2014). Radiative-convective insta-
826 bility. *J. Adv. Model. Earth Syst.*, *6*(1), 75–90. doi: 10.1002/2013MS000270
- 827 Grabowski, W. W. (2006). Impact of explicit atmosphere-ocean coupling on MJO-like
828 coherent structures in idealized aquaplanet simulations. *J. Atmos. Sci.*, *63*(9),
829 2289–2306. doi: 10.1175/JAS3740.1
- 830 Held, I. M., Hemler, R. S., & Ramaswamy, V. (1993). Radiative-convective equi-
831 librium with explicit two-dimensional moist convection. *J. Atmos. Sci.*, *50*(23),
832 3909–3909.
- 833 Hohenegger, C., & Stevens, B. (2016). Coupled radiative convective equilibrium
834 simulations with explicit and parameterized convection. *J. Adv. Model. Earth*
835 *Syst.*, *8*(3), 1468–1482.
- 836 Jeevanjee, N., & Romps, D. M. (2013). Convective self-aggregation, cold pools, and
837 domain size. *Geophys. Res. Lett.*, *40*(5), 994–998. doi: 10.1002/grl.50204
- 838 Khairoutdinov, M. F., & Emanuel, K. A. (2010). Aggregated convection and the reg-
839 ulation of tropical climate. *Preprints, 29th conference on Hurricanes and Tropi-*
840 *cal Meteorology, Tucson, AZ, Amer. Meteor. Soc.*, P2.69.
- 841 Khairoutdinov, M. F., & Randall, D. A. (2003). Cloud resolving modeling of the
842 ARM summer 1997 IOP: Model formulation, results, uncertainties, and sensi-
843 tivities. *J. Atmos. Sci.*, *60*(4), 607–625. doi: 10.1175/1520-0469(2003)060<0607:
844 CRMOTA>2.0.CO;2
- 845 Liu, C., & Moncrieff, M. W. (2008). Explicitly simulated tropical convection
846 over idealized warm pools. *Journal of Geophysical Research: Atmospheres*,
847 *113*(D21). Retrieved from [https://agupubs.onlinelibrary.wiley.com/
848 doi/abs/10.1029/2008JD010206](https://agupubs.onlinelibrary.wiley.com/doi/abs/10.1029/2008JD010206) doi: 10.1029/2008JD010206
- 849 Mauritsen, T., & Stevens, B. (2015, May). Missing iris effect as a possible cause of
850 muted hydrological change and high climate sensitivity in models. *Nature Geo-*
851 *science*, *8*(5), 346–351. doi: 10.1038/ngeo2414
- 852 Muller, C. J., & Bony, S. (2015). What favors convective aggregation and why?
853 *Geophys. Res. Lett.*, *42*(13), 5626–5634. doi: 10.1002/2015GL064260
- 854 Muller, C. J., & Held, I. M. (2012). Detailed investigation of the self-aggregation of
855 convection in cloud-resolving simulations. *J. Atmos. Sci.*, *69*, 2551–2565. doi:
856 10.1175/JAS-D-11-0257.1
- 857 Mller, S. K., & Hohenegger, C. (2020). Self-aggregation of convection in spa-
858 tially varying sea surface temperatures. *Journal of Advances in Model-*
859 *ing Earth Systems*, *12*(1), e2019MS001698. Retrieved from [https://
860 agupubs.onlinelibrary.wiley.com/doi/abs/10.1029/2019MS001698](https://agupubs.onlinelibrary.wiley.com/doi/abs/10.1029/2019MS001698)
861 (e2019MS001698 10.1029/2019MS001698) doi: 10.1029/2019MS001698
- 862 Nakajima, K., & Matsuno, T. (1988). Numerical experiments concerning the origin
863 of cloud clusters in the tropical atmosphere. *Journal of the Meteorological Soci-*
864 *ety of Japan. Ser. II*, *66*(2), 309–329. doi: 10.2151/jmsj1965.66.2_309
- 865 Naumann, A. K., Stevens, B., & Hohenegger, C. (2019). A moist conceptual model
866 for the boundary layer structure and radiatively driven shallow circulations in
867 the trades. *J. Atmos. Sci.*, *76*(5), 1289–1306.
- 868 Naumann, A. K., Stevens, B., Hohenegger, C., & Mellado, J. P. (2017). A concep-
869 tual model of a shallow circulation induced by prescribed low-level radiative
870 cooling. *J. Atmos. Sci.*, *74*(10), 3129–3144.
- 871 Neelin, J. D., & Held, I. M. (1987). Modeling tropical convergence based on the
872 moist static energy budget. *Monthly Weather Review*, *115*(1), 3–12.
- 873 Pierrehumbert, R. T. (2010). *Principles of planetary climate*. Cambridge University
874 Press.
- 875 Raymond, D. J., Sessions, S. L., Sobel, A. H., & Fuchs, Ž. (2009). The mechanics of
876 gross moist stability. *J. Adv. Model. Earth Syst.*, *1*(3).

- 877 Romps, D. M. (2011). Response of tropical precipitation to global warming. *J. Atmos. Sci.*, *68*(1), 123–138.
- 878
- 879 Semie, A. G., & Tompkins, A. M. (2016). Organization of tropical convection in low
880 vertical wind shears: impact of boundary conditions. In *Egu general assembly
881 conference abstracts* (Vol. 18).
- 882 Shamekh, S., Muller, C., Duvel, J.-P., & D’Andrea, F. (2019). How do ocean warm
883 anomalies favor the aggregation of deep convective clouds? *J. Atmos. Sci.*
- 884 Singh, M. S., & O’Gorman, P. A. (2012). Upward shift of the atmospheric general
885 circulation under global warming: theory and simulations. *J. Climate*.
- 886 Sobel, A. H., Nilsson, J., & Polvani, L. M. (2001). The weak temperature gradient
887 approximation and balanced tropical moisture waves. *J. Atmos. Sci.*, *58*, 23.
888 doi: 10.1175/1520-0469(2001)058<3650:TWTGAA>2.0.CO;2
- 889 Tompkins, A. M. (2001). Organization of tropical convection in low vertical wind
890 shears: The role of water vapor. *J. Atmos. Sci.*, *58*(6), 529–545. doi: 10.1175/
891 1520-0469(2001)058<0529:OOTCIL>2.0.CO;2
- 892 Tompkins, A. M., & Craig, G. C. (1998). Radiative-convective equilibrium in a
893 three-dimensional cloud-ensemble model. *Quart. J. Roy. Meteor. Soc.*, *124*,
894 2073–2097. doi: 10.1002/qj.49712455013
- 895 Wing, A. (2019). Self-aggregation of deep convection and its implications for cli-
896 mate. *Current Climate Change Reports*, *5*(1), 1–11.
- 897 Wing, A., & Cronin, T. W. (2016). Self-aggregation of convection in long channel
898 geometry. *Quart. J. Roy. Meteor. Soc.*, *142*(694), 1–15. doi: 10.1002/qj.2628
- 899 Wing, A., & Emanuel, K. (2014). Physical mechanisms controlling self-aggregation
900 of convection in idealized numerical modeling simulations. *J. Adv. Model.
901 Earth Syst.*, *6*(1), 59–74. doi: 10.1002/2013MS000269
- 902 Wing, A., Emanuel, K., Holloway, C., & Muller, C. (2017). Convective self-
903 aggregation in numerical simulations: A review. *Surv. Geophys.*, *38*(6),
904 1173–1197. doi: 10.1007/978-3-319-77273-8_1
- 905 Yang, D. (2018). Boundary layer diabatic processes, the virtual effect, and convec-
906 tive self-aggregation. *Journal of Advances in Modeling Earth Systems*, *10*(9),
907 2163–2176. Retrieved from [https://agupubs.onlinelibrary.wiley.com/
908 doi/abs/10.1029/2017MS001261](https://agupubs.onlinelibrary.wiley.com/doi/abs/10.1029/2017MS001261) doi: 10.1029/2017MS001261